Article:
Oloyede, O, Bigg, TD, Cochrane, RF et al. (1 more author) (2016) Microstructure evolution and mechanical properties of drop-tube processed, rapidly solidified grey cast iron. Materials Science and Engineering A, 654. pp. 143-150. ISSN 0921-5093

https://doi.org/10.1016/j.msea.2015.12.020

Microstructure evolution and Mechanical properties of drop-tube processed, rapidly solidified grey cast iron

Olamilekan Oloyede[1]*, Timothy D. Bigg[1], Robert F. Cochrane[1], Andrew M. Mullis[1]

[1]Institute for Materials Research, School of Chemical and Process Engineering, University of Leeds, Leeds LS2 9JT

*Corresponding author: Tel.: +44 113 343 2568
Email addresses: pmoro@leeds.ac.uk (O.R. Oloyede), a.m.mullis@leeds.ac.uk (A.M. Mullis)

Abstract

The microstructure, phase composition and microhardness of rapidly solidified grey cast iron BS1452 Grade 250 are compared against the conventionally solidified alloy. Powder samples were prepared using containerless processing via the drop-tube technique. The rapidly cooled droplets were collected and sieved into size range from ≥ 850 μm to ≤ 53 μm diameters corresponding to estimated rates of 200 K s^{-1} to 23,000 K s^{-1}. Microstructure evaluations were made by optical and scanning electron microscopy, while XRD was used for identification and analysis of evolved phases. The control sample showed extensive graphite flake formation which was absent in virtually all the droplets samples. With decreasing particle size (increasing cooling rate) we observed an increase in the proportion of Fe_3C present and the retention of γ-Fe in preference to α-Fe, with the proportion of retained austenite increasing with increasing cooling rate. At the highest cooling rates utilised a Martensitic or acicular ferrite structure was observed. Cooling rates of 200 K s^{-1} resulted in a doubling of the measured microhardness relative to the as-received (slowly cooled) material. Cooling at the highest rates achieved resulted in a further doubling of the measured microhardness.

Keywords: Rapid solidification, Drop tube, Grey cast iron, Cooling rate, Microstructure, Microhardness

1. Introduction

Grey cast iron remains one of the most important casting materials, with over 70% of the total world's production tonnage [1]. The ultimate structure of this Fe-C-Si based alloy depends primarily on its composition and the cooling rate applied during shaping [2]. Generally, under 'normal' solidification conditions, slow cooling permits the formation of extensive flake graphite and as a result of this, the material may suffer from poor mechanical properties, particularly low ductility and a tendency towards brittle failure [3-4]. However, with recent developments in rapid solidification technology, methods such as containerless processing may be applied to control the cooling rate of the alloy for any given elemental composition [5]. This leads to modification of the morphology, size and distribution of the flake graphite and of the structure of the matrix, potentially giving rise to improved mechanical properties for the material [6].

Generally, cast irons are relatively high carbon alloys which are classified mainly as grey, ductile or white based upon the shape of graphite in grey and ductile irons and the existence of carbides in white irons. Graphite in grey iron appears as randomly distributed flakes but is

nodular in ductile iron. Grey and ductile cast iron usually also contain some Si or other alloying additions, which act as stabilizers for the graphite, such that it precipitates out even at hypoeutectic compositions.

Grey cast iron, which is so called, not because of its colour, but due to the unreflective appearance of its fractured surface, is widely chosen in many industrial applications because of its flexibility in usage, good castability, low-cost (20-40% less than steel), corrosion resistance, machinability and low melting point. It also displays a high damping capacity due to its high carbon content, which gives it an advantage in modern automotive part manufacture. Conventional grey cast iron has a pearlite matrix and it is used extensively in the production of machine components such as disc brake rotors, gear bearings, engine casings and hydraulic valves [7, 8, 9].

Very limited investigations on the rapid solidification of grey cast iron have been undertaken to date. Behnam et al. [7] have studied the effect of cooling rate on primary dendrite arm spacing (DAS), secondary dendritic arm spacing (SDAS), thickness of ferrite-cementite layer (λ_e) and mechanical property (hardness) of grey cast iron. Their evaluation was that, as expected, higher cooling rates resulted in smaller DAS, SDAS and λ_e. The DAS was found to be related to the cooling rate, R, via a power law relationship with DAS $\propto R^{-0.61}$. λ_e was also found to follow a power law relationship, albeit with the smaller negative exponent of -0.16. These were found to correlate with hardness data via a quadratic relationship, with the hardness increasing by ~33 % as the cooling rate was increased from 0 to 20 K s^{-1}. Another significant effort was made by Kiani-Rashid et al. [10], in which they outlined the effect of cooling rate on the formation of metastable phases in austempered nickel-molybdenum grey cast iron and how this affected its microhardness. Yang et al. [11], in a study of gas atomized grey cast iron powders, related the microstructural evolution of the powders to the particle size (and hence cooling rate). They showed that with increasing cooling rate there was a change in the flake morphology from random to oriented. Moreover, from their XRD analysis it was evident that with increasing cooling rate (decreasing particle size) the proportion of γ-Fe increased while that of α-Fe decreased. However, there was no evidence, either from their XRD or microstructural analysis, of any phases other than ferrite, austenite and Fe_3C.

In a study by Yi et al. [12]based on repair technology using the rapid solidification process of laser fusion welding, they discovered that overall crack toughness of the material can be increased around the repaired zone (RZ). This was further explained by Ebrahimnia et al. [13] who stated that cracks initiate mostly at the interface of graphite and then propagate through the matrix of a component thereby causing fracture. However they show that with laser processing this can be curtailed. As further established by Fu et al. [14], their results showed that the weldability of cast iron can be improved by laser cladding by inhibiting graphite precipitation at the interface between the weld zone and the pre-existing material.

The purpose of this investigation is to produce rapidly solidified grey cast iron powders using a conventionally cast BS1452 Grade 250 ingot as the feedstock material. The microstructure and microhardness of the powders will then be assessed as a function of cooling rate and compared to that of the conventionally solidified feedstock material. Drop-tube processing is used for this purpose, it being a containerless processing technique by which rapid solidification of small droplets in-flight is achieved. As such it is an analogue for the commercial high pressure gas atomization technique. This method is such that the cooling rate will increase in a predictable manner as the particle size decreases. Moreover, due to the increased rate of cooling, together with melt sub-division effects, the droplet undercooling will also increase with decreasing droplet size, albeit in a stochastic manner. This paper thereby presents results to show the dependence of the microhardness on the microstructure and phase evolution as a result of rapid solidification processing of grey cast iron.

2. Experimental Procedure

Conventionally solidified, low alloy commercial grey cast iron to specification BS1452 Grade 250 was supplied as continuously cast 25 mm x 1000 mm round bar by West Yorkshire Steel. Table 1 confirms the compositional analysis obtained for the alloy by XRF analysis and also gives the notional specification for grey cast iron, showing that all elemental constituents are within the range as prescribed by the ASM international standard [15]. The inoculant used in the supplied material was Supanoc (Si 70.51%; Al 1.64%; Ca 1.39%, balance Fe) which was added at the rate of 4 kg/T into the metal stream when pouring into the distribution ladle. The carbon equivalent (CE) value shows that the alloy is hypoeutectic, with its equivalent carbon content being less than 4.3 %. The Calphad software package MTDATA was used to assess the equilibrium behaviour of the Fe-C-Si-P system with composition as given below, in order to confirm that the system was hypoeutectic, as per the simple equivalent carbon calculation.

This material was used as feedstock for the drop-tube experiments and also served as a reference material against which the effects of rapid solidification could be evaluated. To obtain rapidly solidified droplets from the bulk as-cast sample, small pieces weighing approximately 16 g were cut from the ingot and placed in an open-top alumina crucible with 3 laser drilled, 300 µm diameter, holes in the base. When the crucible is pressurised the melt is ejected through these holes to fall freely through the 6.5 m length of the drop-tube, wherein they undergo rapid cooling and solidify in-flight.

Table 1: Elemental composition of commercial grey cast iron BS1452 grade 250 by XRF.

Element (wt.%)	**C**	**Si**	**Mn**	**P**	**S**	**Fe**	**CE**
BS 1452 Grade 250	2.70	2.83	0.58	0.15	0.054	93.34	3.70
ASTM A48 specification	2.5-4.0	1.0-3.0	0.2-1.0	0.002-1.0	0.02-0.025	96.28-90.96	Cal.

Figure 1 shows a schematic illustration of the drop-tube apparatus used in this study. At the top of the drop-tube is the furnace used to melt the metal and produce the spray of droplets. The crucible sits inside a graphite susceptor which makes a pressure tight seal with the top flange on the tube, allowing it to be pressurised when the melt is to be ejected. The susceptor, which sits inside an alumina radiation shield, is induction heated using a 3 kW RF generator. Prior to melting the entire apparatus is evacuated and purged according to the following schedule: (i) firstly the tube is evacuated to a pressure of ~ 1 Pa (0.01 mbar) using a 2-stage, oil-filled rotary vain (roughing) pump and then flushed with oxygen free N_2 gas at a pressure of 40 kPa (400 mbar); (ii) step (i) is repeated 3 times; and (iii) the tube was then further evacuated to ~ 10^{-4} Pa (10^{-6} mbar) using a turbo-molecular pump before being refilled to 40 kPa with oxygen free N_2 gas. The pressures in the tube are monitored by a cold cathode ionisation gauge, a Pirani gauge and a capacitance manometer. Heating and cooling of the system was monitored using an R-type thermocouple inside the melt crucible. When the desired superheat was achieved the melt was ejected by pressurizing the crucible with 0.4 MPa of N_2 gas. Following ejection the melt cools and solidifies into near spherical droplets of different sizes during free-fall in the tube. The resulting particles were collected after cooling and sieved into 10 standard diameter ranges, namely > 850 µm, 850-500 µm, 500-300 µm, 300-212 µm, 212-150 µm, 150-106 µm, 106-75 µm, 75-53 µm, 53-38 µm and < 38 µm.

These were then hot mounted in Transoptic resin for XRD analysis and conductive Probemet-Cu loaded resin for microscopic examination, as were small sections of the as-received ingot.

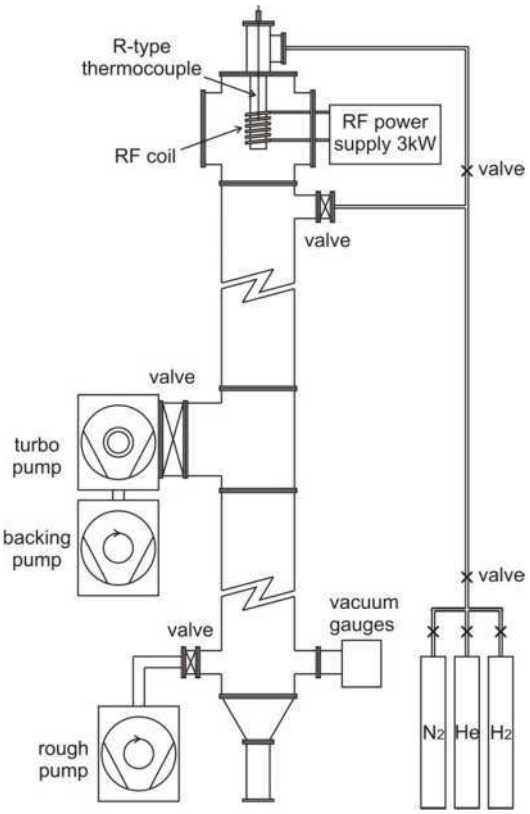

Figure 1: Schematic diagram of the drop-tube apparatus used in this study.

The mounted samples were ground using a series of progressively finer SiC papers starting with 240, 400, 800 and lastly 1200 grit. After each grinding stage the samples were washed using dilute detergent, running water and then methanol and thereafter dried with hot air. Optical microscopy was used at the end of each stage to check and confirm the quality of the surface finish before proceeding to the next finer grade of grinding media. The samples were then polished using 6 µm, 3 µm, and 1 µm diamond paste in progression to obtain the level of surface finish required for microstructural examination. Again, after each polishing stage the samples were washed using dilute detergent, running water and then methanol and thereafter dried with hot air and checked using optical microscopy. For cast iron, etching standard PN-61/H-0503 recommends 2 % nitric acid in 98% ethanol (Nital) solution [16], which has been adopted here. Alkaline sodium picrate and Murakami's reagent were also evaluated for this purpose, but as the results obtained were generally inferior to those obtained with Nital their use was not pursued.

The microstructures of the samples were examined using an Olympus BX 51 optical microscope and an EVO scanning electron microscopy with in-built energy-dispersive x-ray analyser (EDX). The optical microscope is fitted with a 10 times eyepiece and six objectives (5, 10, 20, 50 and 100 times). A Zeiss Axiocam MRC5 digital camera is fitted at the top for image capture. The EVO-SEM was operated between 10 – 20 kV using both secondary electron and back-scatter detection at different magnifications. The constituent phases of the samples were identified using a PANalytical Diffractometer with Cu K_α radiation at room temperature.

Microhardness measurements, using loads in the range 0.01 - 0.05 kg, were carried out on mounted and polished samples using a TUKON™ 1202 Wilson Hardness (Vickers) analyser

at ambient conditions. In order to ensure that the measurements were characteristic of the sample material only, and not of the mounting compound, measurements were made on samples mounted in Transoptic mounting compound, Bakelite and Cu loaded Bakelite. As no significant difference was observed between the different mounting media we conclude that the microhardness values are indicative of the sample droplets, and are not influenced by the mount. Each measurement was repeated a minimum of 10 times.

3. Results

3.1 Thermodynamic Modelling

Based on a simple equivalent carbon calculation we would estimate the liquidus temperature of this alloy to be 1492 K, some 70 K above the Fe-C eutectic temperature. For the alloy with composition as in Table 1, the Calphad calculation gives the liquidus temperature as 1521 K and predicts that the eutectic temperature increases by around 15 K for a Si concentration of 2.83 wt.%. However, [17] have pointed out significant difference between the stable and metastable Fe-C-Si phase diagrams, in particular relating to the role of Si which can depress the eutectic temperature under rapid cooling conditions. Under rapid cooling, the effect of a 2.83 wt.% addition of Si, estimated from [17], could be to lower the eutectic temperature by up to 65 K, relative to the equilibrium value for the same Si concentration.

The anticipated effects of rapid solidification processing by drop-tube processing can consequently be summarised as follows:

1) The post-solidification motion of C in the solid-state will be suppressed. This will result in more carbon remaining in solution within the Fe dendrites, which will either remain as γ (i.e. the solid-state decomposition, $\gamma \rightarrow \alpha$, will be suppressed, giving retained austenite) or which will transform to α, albeit highly supersaturated in C.
2) In the presence of Si the eutectic temperature will be suppressed, giving a larger L + γ stability field. This will increase the volume fraction of γ that might be expected, at the expense of the γ + cementite eutectic (Fe_3C).
3) The combined effects of high cooling rate and melt sub-division experienced in the smaller droplet size fractions may lead to melt undercooling [18], even in the presence of an inoculant. Where the undercooling is larger than the liquidus-eutectic interval this will lead to a further increase in the fraction of primary γ-phase dendrites, at the expense of the γ + cementite eutectic. However, unlike cooling rate, which is a deterministic function of particle size, undercooling is stochastic and its effects are therefore more difficult to assess.

The likely upshot is that at moderate to high cooling rate (< 300 μm diameter) an increase in the volume fraction of primary Fe dendrites and a decrease in the volume fraction of the eutectic matrix might be expected as a consequence of rapid cooling.

3.2. Cooling rate determination for drop-tube processed grey cast iron.

The cooling rate of droplets during free-fall in the drop-tube can be estimated based on the heat transfer from the droplet [19, 20]. The starting point for modelling the cooling rate is the balance of heat fluxes for a given droplet, which can be expressed as

$$\frac{dT_d}{dt}\left[c_l(1-f)+c_s f - L\frac{df}{dt}\right] = \frac{6h}{\rho d}(T_d - T_g) + \frac{6\varepsilon\sigma_b}{\rho d}(T_d^4 - T_g^4) \qquad (1)$$

where T_d is the instantaneous temperature of the particle, c_l and c_s are the specific heat of the metal in the liquid and solid states respectively; f is the solid fraction, ρ the density of the metal, d the diameter of the droplet, ε the emissivity of the droplet surface, σ_b the Stefan-Boltzman constant and T_g the temperature of the gas. The heat transfer coefficient, h, is normally estimated from

$$h = \frac{\kappa_g}{d}\left(2 + 0.6\sqrt{\mathrm{Re}}\sqrt[3]{\mathrm{Pr}}\right) \tag{2}$$

where κ_g is the thermal conductivity of the gas and Re and Pr are the Reynolds and Prandtl numbers for the flow, which are given by:

$$\mathrm{Pr} = \frac{c_{pg}\mu}{\kappa_g}, \qquad \mathrm{Re} = \frac{\rho_g d}{\mu}\left|v_d - v_g\right| \tag{3}$$

where c_{pg} is the specific heat capacity of the gas, μ is its kinematic viscosity and $|v_d - v_g|$ is the differential velocity between the droplet and the gas. This we assume is the terminal velocity, v_T, for the particle of diameter, d, under the conditions prevailing in the tube. For a spherical droplet, including buoyancy effects this is given by:

$$\left|v_d - v_g\right| = v_T = \sqrt{\frac{4gd}{3C_d}\left(\frac{\rho - \rho_g}{\rho_g}\right)} \tag{4}$$

where ρ_g is the density of the gas, g is the acceleration due to gravity and C_d is the drag coefficient, which we estimate from:

$$C_d\,\mathrm{Re}^2 = \frac{4mg\rho_g}{\pi\mu^2} \tag{5}$$

where m is the mass of the droplet.

Based on the measured composition of the sample and the subsequent Calphad calculation the liquidus temperature has been estimated as 1521 K and the cooling rate evaluation is based on the average cooling rate between the liquidus and the metastable Fe-C-Si eutectic temperature (estimated at 1353 K). T_g has been taken as 298 K. The thermophysical parameters of N_2 gas and grey cast iron are as shown in Table 2.

The calculated cooling rate for the droplets as a function of their diameter, d, is shown in Figure 2 and range from 200 K s^{-1} for a 850 µm droplet to ~ 23,000 K s^{-1} for a 38 µm droplet. The corresponding terminal velocities in the tube range from ~ 2 m s^{-1} for a 38 µm droplet to ~ 15 m s^{-1} for an 850 µm droplet. As with most previous such calculations of cooling rates for particles in-flight [21, 22], the cooling rate is well approximated by a power law fit, as shown in Figure 2. The cooling rates calculated are lower (typically by around a factor of 3) than those calculated in [21], also for drop-tube cooling. This is accounted for by their use of He as a cooling medium, the thermal conductivity of He being significantly higher than that of the N_2 gas used in this study.

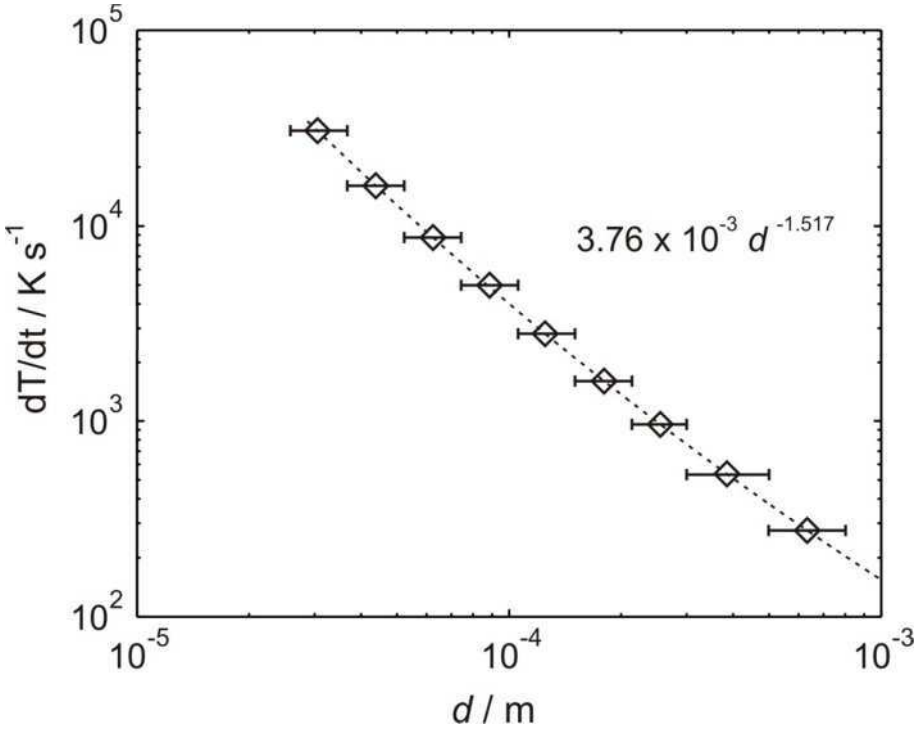

Figure 2: Estimated cooling rate of droplets as a function of their diameter. Markers show the boundaries of the size fractions used in this study.

Table 2: The thermophysical parameters of N_2 gas and grey cast iron.

Material	Parameter	Value
Nitrogen gas [23]	c_{pg}	1039 J kg^{-1} K^{-1}
	μ	1.78 x 10^{-5} N s m^{-2}
	κ_g	2.6 x 10^{-2} W m^{-1} K^{-1}
	ρ_g	1.16 kg m^{-3} (at 0.1 MPa)
Grey cast iron [24]	L	1.26 × 10^5 J kg^{-1}
	c_l	495 J kg^{-1} K^{-1}
	ρ	7050 kg m^{-3}

3.3. XRD analysis

Fig. 3 shows the XRD patterns for the rapidly solidified grey cast iron as a function of droplet size. In order to avoid biasing the analysis from the surface of the sample the XRD has been performed on mounted and polished samples in order to reveal the particle interiors. The amorphous transoptic mounting compound produces a broad 'hump' in the response between 20-30º in 2θ, although as most of the peaks of interest occur at angles of 2θ ≥ 35º this is not a serious limitation. However, for this reason graphite peaks in the as-received material around 2θ = 26º have been omitted. Three main phases are identified, ferrite (α), austenite (γ) and cementite (Fe_3C). The as-received material is shown, as expected, to comprise only ferrite and cementite, while all three phases are found to be present in all drop-tube size fractions, albeit in different proportions, as indicated by the different peak heights in

the XRD patterns. It was observed that as the droplets size reduces (i.e. as the cooling rate increases), there is a trend in the phase transformation from α-Fe to γ-Fe and back to an α'-Fe like metastable phase. However, due to the level of noise in the measurements resulting from fluorescence of the Fe in the Cu K_α radiation, it was not possible to conduct a Rietveld refinement to obtain the phase fractions present. Consequently, the transformation of austenite to α'-Fe in the 75-106 µm and 53-75 µm droplets is explored using SEM analysis.

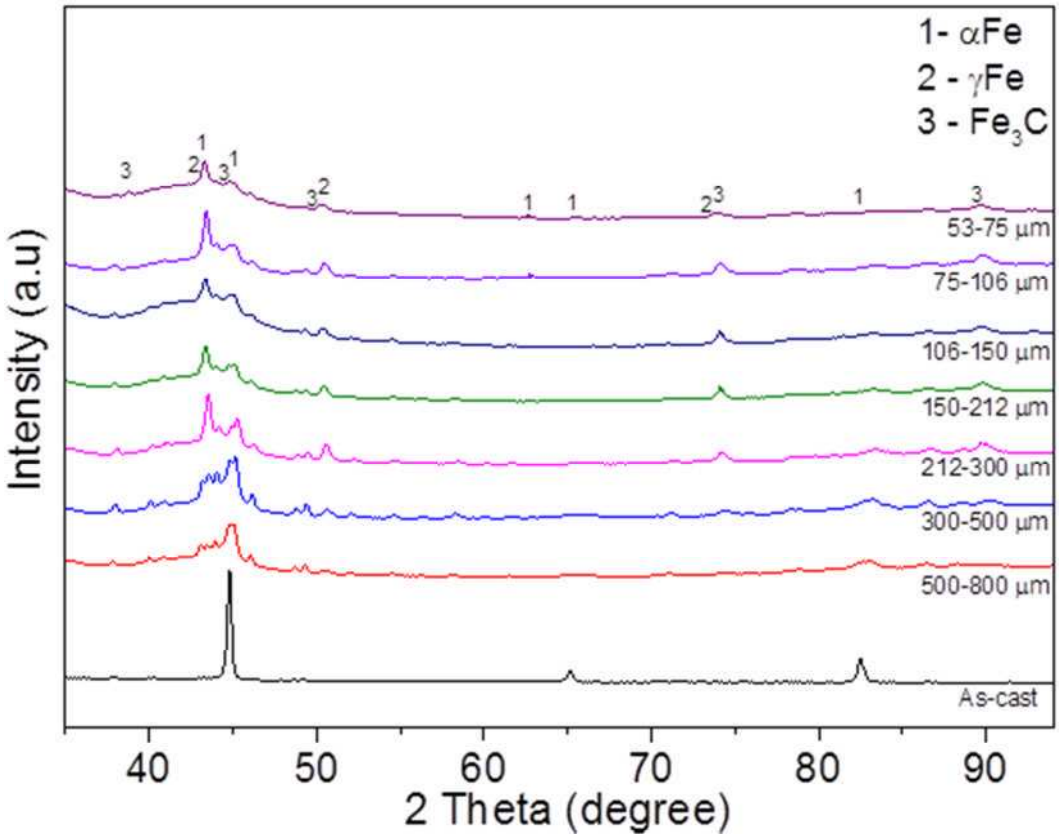

Figure 3: X-ray pattern and phase identification for droplet size ranges 53-75 µm, 75-106 µm, 106-150 µm, 150-212 µm, 212-300 µm, 300-500 µm and 500-800 µm.

3.4. Microstructures and phase identification

Before Etching: Fig. 4 shows (a) optical and (b) SEM images of the unetched, as-cast material displaying extensive flake graphite, typical of the grey cast iron type C morphology [25]. This is indicative of a sample that was slowly cooled, such that there was sufficient time for the graphite to nucleate and grow. The estimated cooling rate for this sample is < 10 K s^{-1}. The observed graphite flakes are not only randomly distributed in the ferrite matrix they intersect each other, thereby providing an easy path for crack propagation in the material, hence the brittle nature of this conventionally solidified grey cast iron. Meanwhile, Fig. 5 shows optical micrographs of selected, unetched size fractions of the drop-tube processed material. It is clear from micrographs that there is no evidence of flake graphite precipitation in any of the drop tube samples, even for the largest droplet sizes, wherein the cooling rate is ~200 K s^{-1}. Hence, even at relatively modest cooling rates, the drop-tube samples are free from graphite flake.

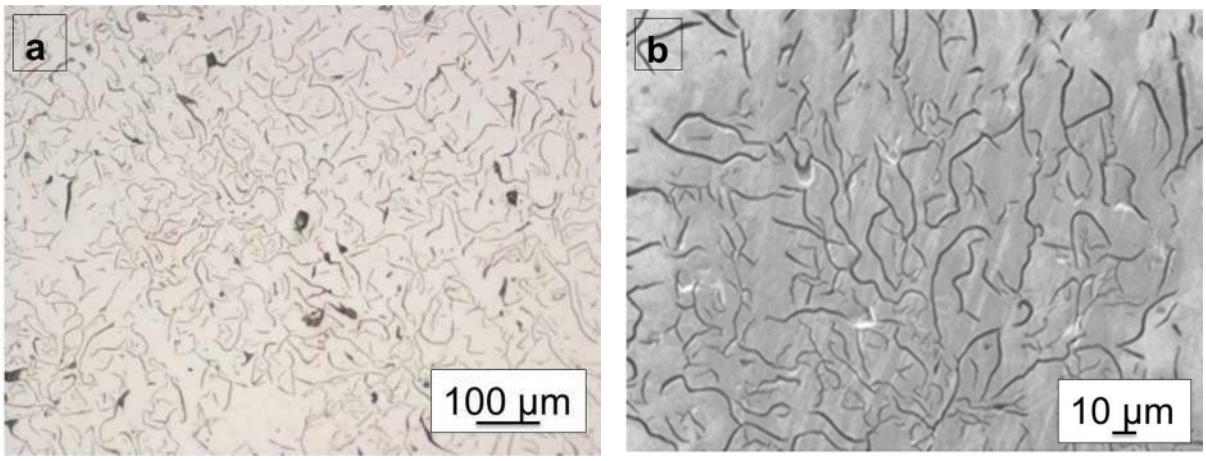

Figure 4: Unetched "as-cast" grey cast iron sample, classified as coarse flake graphite type C in α-Fe (ferrite) matrix.

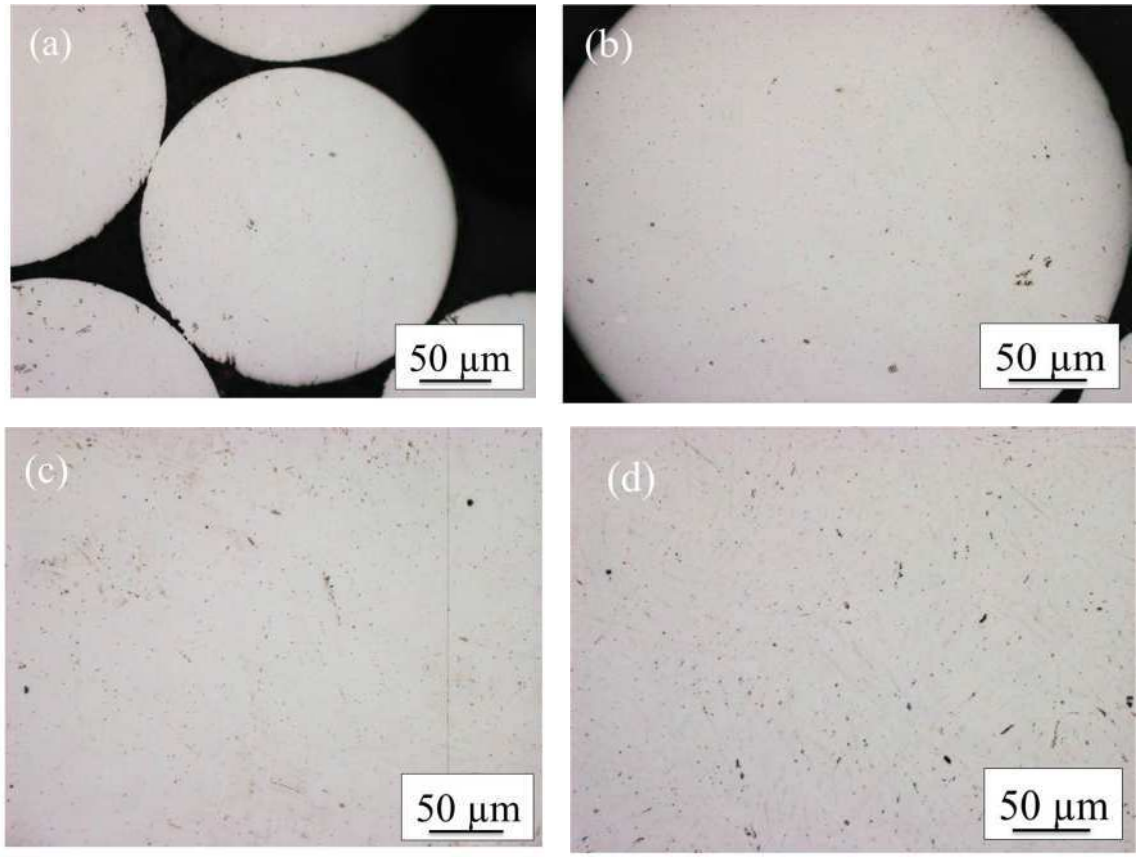

Figure 5: Optical micrographs of unetched drop-tube processed samples in the size ranges; (a) 212 – 300 µm, (b) 300 – 500 µm, (c) 500 – 800 µm and (d) ≥ 850 µm

After Etching: Fig. 6 shows the morphologies of the as-cast and the ≥ 850 µm sample etched in 2% nital respectively. Dendritic Fe, which is the primary solidification phase, and the pearlite eutectic are clearly evident in all samples. A significant reduction in the scale of the microstructure is also evident in the rapidly solidified sample.

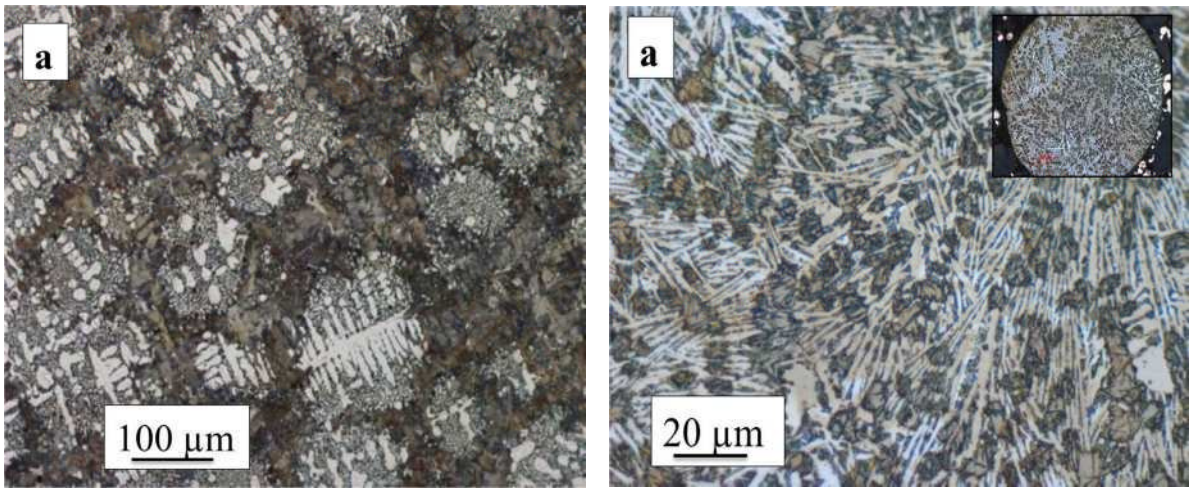

Figure 6: Morphology of (a) as-cast and (b) ≥ 850 droplet samples, after etching in 2% Nital. Primary dendritic Fe and interdendritic pearlite eutectic are both clearly evident.

The effect of cooling rate on the evolving microstructures of the different droplets, and that of the as-cast sample, is shown in Fig. 7. It reveals the morphologies of the samples with clear evidence of reduced microstructural scale as the cooling rate is increased with decreasing particle size. The 4 largest size fractions i.e. ≥ 850 to 300 - 212 µm, shown in Fig. 7 (b - d), reveal relatively similar structures with a strong primary dendritic morphology, although with less fragmentation as the droplet size is reduced. This is particularly apparent when comparing Figure 7b, which shows significant fragmentation, with either Figure 7 c or d, in which fragmentation is virtually absent. Three of the more obvious regions of fragmentation are indicated in Figure 7b, with the fragmentation being evident as an array of secondary arms which have become detached from their primary trunks. Such fragmentation is a consequence of partial remelting and spheroidization of side arms while the solid is in co-existence with the liquid [26], the extent of fragmentation being dependent upon the balance between the time for which the co-existence occurs and the time required for spheroidization. As the time for spheroidization decreases rapidly as the dendrite size decreases, modest increases in cooling rate or undercooling can lead to fragmentation due to scale refinement which is then reversed at high cooling rate when there is insufficient co-existence time.

A further change in the microstructure, which again is most evident when comparing Figure 7b, in which the cooling rate is relatively modest, with (say) Figure 7d, is that the volume fraction of primary dendrites is lower (and consequently the volume fraction of the interdendritic eutectic matrix is higher) at low cooling rate than is the case at higher cooling rates. In fact, due to the good contrast between the primary dendrites and the eutectic matrix after etching, it is possible to estimate the volume fraction of primary dendrites by image analysis to estimate the area fraction of each phase (primary dendrite and eutectic) in the micrographs from each size fraction. For the largest droplet size (800-500 µm, Figure 7b) the volume fraction of the primary dendrite phase is estimated at 59.8%, dropping to 62.1% in the 500-300 µm size fraction and thereafter being approximately constant at ~ 70%. This increase in the primary dendritic phase is consistent with the eutectic temperature dropping and/or the undercooling increasing as the cooling rate increases, as discussed in Section 3.2 above.

For droplets with diameters below 150 µm there is a distinct change in the solidification morphology, with the development of a lath or needle type structure and the loss of the strong orthogonality evident at low cooling rates (compare for instance Figures 7b and 7f). This is particularly evident for droplets with diameters less than 106 µm (Figure 7 g-h), for which

cooling rates are likely to exceed 5000 K s^{-1}. This change in the morphology of the primary dendritic phase is likely to reflect increasing amounts of Martensite being formed during primary solidification.

The morphological evolution observed here with increasing cooling rate is broadly consistent with the XRD data and can be rationalised as follows. At low cooling rate the dominant phases are as predicted by the equilibrium phase diagram, namely α-Fe and pearlite. However, unlike the slowly cooled, as-received material, there is no evidence of flake graphite indicating that the matrix is likely to be highly supersaturated in carbon. For droplets in the 300-212 μm sieve fraction the XRD data reveals a greater propensity towards retained γ-Fe, with a corresponding reduction in the amount of α-Fe present, although there is little signature of this in the microstructure. In the smallest size fractions, and in particular for droplets with diameters < 106 μm, there is a very clear change in the microstructure to a needle or lath like morphology. This coincides with the emergence of stronger peaks at the α-Fe positions in the XRD spectrum and a corresponding reduction in the intensity of the γ-Fe peaks, leading us to believe at high cooling rate we are observing a transformation to either Martensite or acicular ferrite.

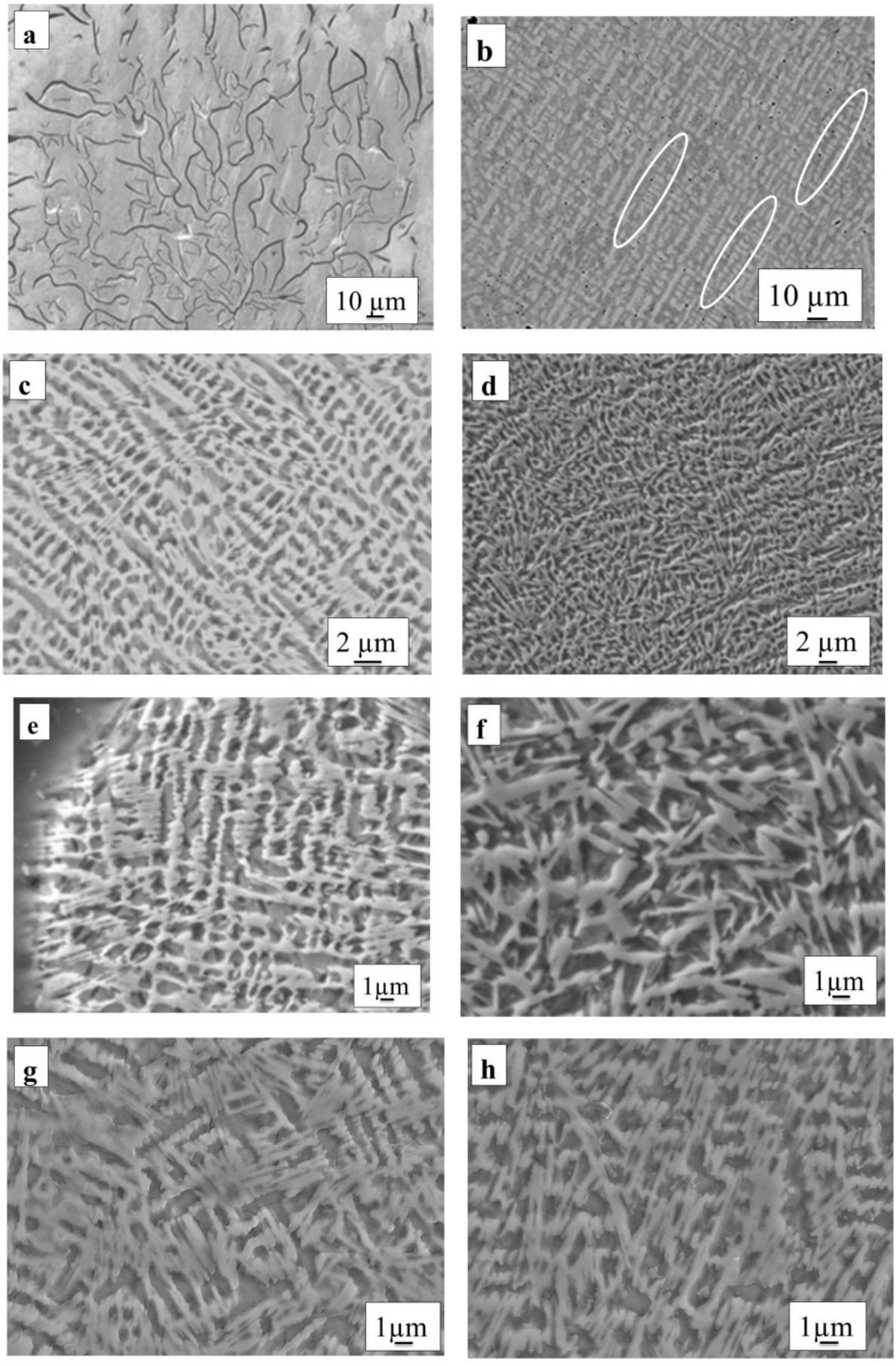
a
10 μm
b
10 μm
c
2 μm
d
2 μm
e
1μm
f
1μm
g
1μm
h
1μm

Figure 7: SEM micrographs of sample microstructures at different particle diameters, corresponding to different cooling rates: (a) as-cast sample revealing extensive flake graphite, (b) 800-500 µm with areas of particular fragmentation highlighted within the ellipses shown, (c) 500-300 µm, (d) 300-212 µm, (e) 212-150 µm, (f) 150-106 µm, (g) 106-75 µm, (h) 75-53 µm. The morphological change in the microstructure for droplets with diameters less the 150 µm is particularly pronounced, with a transition from dendritic to lath or needle like structures.

3.5. Microhardness

To assess the effect of cooling rate, and the consequent change in microstructure, upon mechanical properties, Vickers microhardness measurements have been made on droplets in all size fractions, these being displayed in Figure 8. The minimum hardness, observed in 850 µm diameter droplets, was 704 ± 7 Hv0.05, while the maximum hardness was 1260 ± 4 Hv0.05 in the 38-53 µm sieve fraction. For comparison, the hardness of the matrix of the as-received material was 362 ± 3 Hv0.05. A micrograph of a microhardness indent in the as-received material is shown in Figure 9. As this was the most inhomogeneous of the materials measured, care was taken to ensure no part of any indent impinged upon flake graphite. The trend is both clear and dramatic. Rapid solidification, even at modest cooling rates of ~200 K s^{-1}, results in an approximate doubling of the microhardness, relative to the as-received material. This we can likely ascribe to the α-Fe matrix being highly supersaturated in carbon, as evidenced by the lack of flake graphite precipitation.

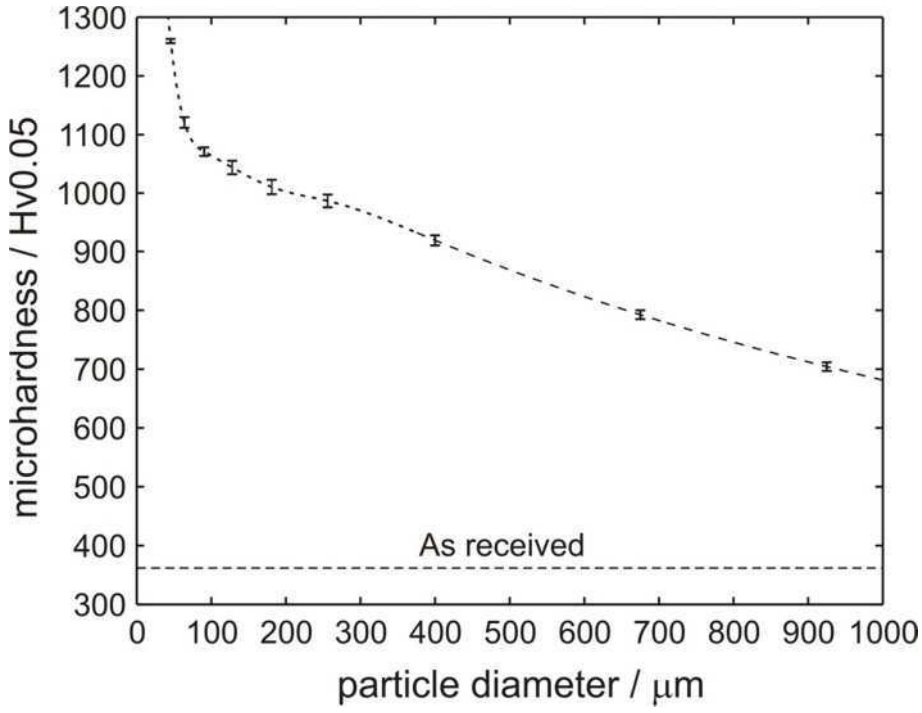

Figure 8: Microhardness value (in Hv0.05) as a function of droplet diameter.

Increased cooling rates result in a steady increase in microhardness, this being most likely related to increasing fractions of retained austenite with a corresponding decrease in the fraction of ferrite present. This is the case until we reach the 106 µm droplets, wherein there

is a steep rise in hardness, which is most likely attributable to a change in the solidification morphology, with the onset of either Martensite or acicular ferrite formation.

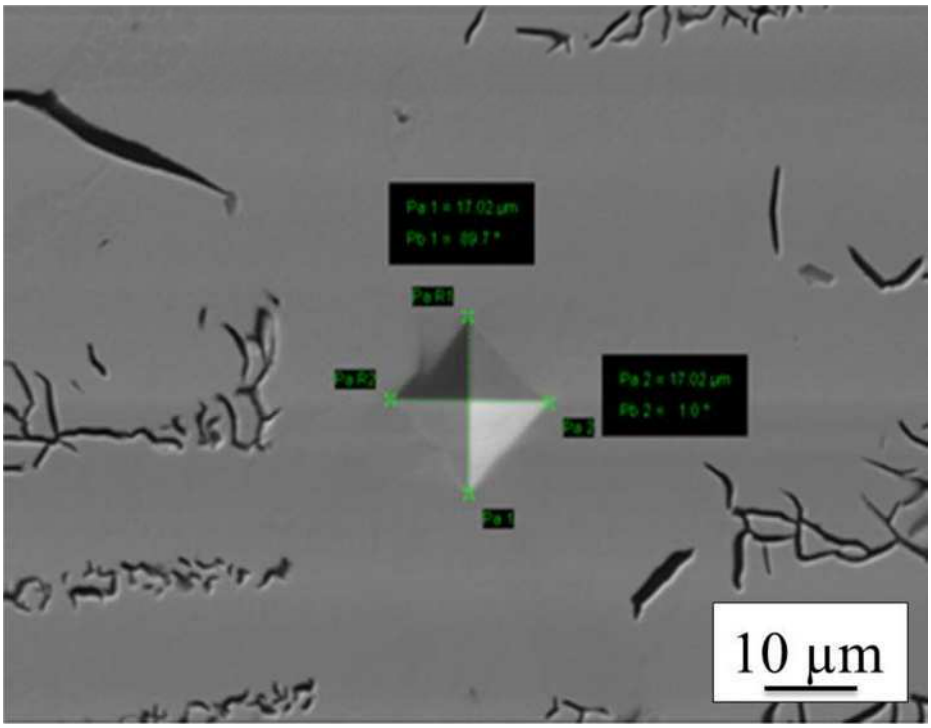

Figure 9: SEM micrograph of the Vickers microhardness indentation in a sample of the as-received grey cast iron.

4.0. Conclusion

Evidence has been presented in this paper by means of metallography and phase analysis on how rapid solidification processing affects the microstructure and mechanical property of commercial grey cast iron at constant elemental composition. The optical and SEM micrographs obtained in the course of this study along with XRD result showed that the structure of conventionally cooled, low-alloy, commercial grey cast iron is ferritic with a well-defined flake graphite network embedded randomly in the Fe matrix. This typical microstructure of slowly cooled grey cast iron may be engineered using rapid solidification processing techniques and the evolved microstructures impact on the mechanical property of the powder particles produced. Even modest rapid solidification cooling rates inhibit the formation of flake graphite, resulting in a near doubling of the measured microhardness. Further increases in cooling rate result in a change to the phase composition, giving first more retained austenite and at the highest cooling rates studied either Martensite or acicular ferrite. This results in a second near doubling of the measured microhardness.

Acknowledgement

This research was carried out in the Institute for Materials Research, University of Leeds. The authors want to thank Dianne Cochrane for metallography, Stuart Micklethwaite and John Harrington for their support in the conduct of electron microscopy. Olamilekan Oloyede

was financially supported by PTDF from Nigeria Federal Government, to whom he is grateful.

References

[1] D.M. Stefanescu; Mater. Sci. Eng. A A413-414 (2005) 322 – 333.
[2] J. Gao and B. Wei; J. Alloys Compd. 285 (1999) 229 – 232.
[3] Metals Handbook, 9th ed., ASM, Metals Park, OH, 1978, vol. 1, pp. 85 – 87.
[4] H. T. Angus; Cast Iron: Physical and Engineering Properties, Butterworth & Co. Ltd., London, Great Britain, 1976, p. 245.
[5] L. Battezzati, M. Baricco and S. Curiotto; Acta Materialia 53 (2005) 1849 – 1856.
[6] K. Brandenberg, K.L. Hayrynen and J.R. Keough; Gear Technol. 18 (2001) 42.
[7] M.M.J. Behnam, P. Davami and N. Varahram; Mater. Sci. Eng. A 528 (2010) 583 – 588.
[8] A. Avci, N. Ilkaya, S. Mehmet and A. Ahmet; J. Mater. Process. Technol. 209(3) (2009) 1410 – 1416.
[9] W. Wei, J. Tianfu, G. Yuwei, Q. Guiying and Z. Xin; J. Mater. Process. Technol. 182 (1-3) (2007) 593 – 597.
[10] A.R. Kiani-Rashid, M. Mostafapour, S.F. Kaboli-Mallak and A. Babakhani; Inter. Scholarly Research Network, 2011 (923241), page 5.
[11] M. Yang, Y. Dai, C. Song and Q. Zhai; J. Mater. Process. Technol. 210 (2010) 351 – 355.
[12] P. Yi, P. Xu, C. Fan, G. Yang, D. Liu and Y. Shi; The Scientific World Journal, 1155 (2014) 541569.
[13] M. Ebrahimnia, F.M. Ghaini, Sh. Gholizade, et al; Materials & Design, 33 (2012) 551 – 556.
[14] W. Fu, Q. Deng, P. Cao, D. Chen, (2014, November). Experimental Research and Engineering Application of Laser Cladding Reparations. In 2014 International Conference on Mechatronics, Electronic, Industrial and Control Engineering (MEIC-14). Atlantis Press.
[15] J.M. Radzikowska; ASM Handbook, vol. 9 (2004) 565.
[16] J. Radzikowska; Adv. Mat. Pro. 157 (2) (2000) 29.
[17] J. Lacaze and B Sundman; Metall. Trans. A 22 (1991) 2211 – 2223.
[18] L. Cao, R.F. Cochrane and A.M. Mullis; Metall. Mater. Trans. A 46 (2015) 4705 – 4715.
[19] N. Zeoli, S. Gu and S. Kamnis; Int. J. Heat. Mass. Transf., 51 (2008) 4121 – 4131.
[20] S. He, Y. Liu and S. Guo; Rare Metal Mater. Eng., 38 (2009) 353 – 356.
[21] G. Kasperovich, T. Volkmann, L. Ratke and D. Herlach; Metall. Mater. Trans. A 39 (2008) 1183.
[22] A.M. Mullis, L. Farrell and R.F, Cochrane; Metall. Mater. Trans. B 44 (2013) 992 – 999.
[23] E.S. Lee and S. Ahn; Acta Metall. Mater. 42 (9), 3231 – 3243.
[24] Casting Handbook (Casting Iron), 1st Ed. Machinery Industry Press, 1993, p 750.
[25] M. Cluhan; Metal Handbook 15 (1988) ASM 629 – 646.
[26] M. Schwarz, A. Karma, K. Eckler and D.M. Herlach; Phys. Rev. Lett. 73 (1994) 1380 – 1383.